Journal of
*Composites Science*

MDPI

*Article*

# Particularities on the Low-Velocity Impact Behavior of 3D-Printed Sandwich Panels with Re-Entrant and Honeycomb Core Topologies

**Andrei Ioan Indreș [1], Dan Mihai Constantinescu [2,*], Oana Alexandra Mocian [1] and Ștefan Sorohan [2]**

[1] Faculty of Aircraft and Military Vehicles, Military Technical Academy "Ferdinand I" of Bucharest, 050141 Bucharest, Romania; andrei.indres@mta.ro (A.I.I.); oana.mocian@mta.ro (O.A.M.)
[2] Department of Strength of Materials, National University of Science and Technology Politehnica Bucharest, 060042 Bucharest, Romania; stefan.sorohan@upb.ro
* Correspondence: dan.constantinescu@upb.ro

**Abstract:** This work describes, through experimental and numerical investigations, the mechanical behavior and energy absorption characteristics of 3D-printed sandwich panels with cellular cores subjected to low-velocity impact. Using fused deposition modeling techniques (FDM), three different sandwich panels, one with a regular hexagonal core and two with re-entrant cores at 0 and 90 degrees, were fabricated. The sandwich panels were subjected to low-velocity impact, at impact energies of 10 J and 15 J. A comprehensive investigation of the panels' behavior through experimental testing and numerical simulation was conducted. The results indicate that the sandwich panel with a 90 degrees re-entrant core is stiffer and absorbs the largest amount of impact energy but, at the same time, suffers significant damage to the upper facesheet. The 0 degrees re-entrant core is compliant and provides both impact resistance and good energy absorption characteristics. Such a sandwich panel finds its application in the construction of personal protective equipment, where the aim is to minimize the forces transmitted during low-velocity impacts and maximize the total absorbed energy. Re-entrant core sandwich panels prove to be very good candidates for replacing the honeycomb core sandwich, depending on the desired engineering application.

**Keywords:** low-velocity impact; re-entrant core; digital image correlation; drop tower impact testing



**Citation:** Indreș, A.I.; Constantinescu, D.M.; Mocian, O.A.; Sorohan, Ș. Particularities on the Low-Velocity Impact Behavior of 3D-Printed Sandwich Panels with Re-Entrant and Honeycomb Core Topologies. *J. Compos. Sci.* **2024**, *8*, 426. https://doi.org/10.3390/jcs8100426

Academic Editors: Mourad Nachtane and Marwane Rouway

Received: 12 September 2024
Revised: 1 October 2024
Accepted: 11 October 2024
Published: 15 October 2024



## 1. Introduction

Sandwich panels have proven to be among engineers' favorite options when aiming to reduce weight, maintain load-carrying capacity and increase energy absorption at the same time. Their usage is extremely popular in aeronautics, aerospace, automotive, maritime and construction industries because of their excellent strength compared to their weight and their behavior under impact loadings [1–5]. Impacts can range from the most common at low velocity, such as an object falling, to high velocity, such as hailstones on aircraft. Low-velocity impact has a special interest because it can induce internal, less localized damage that, over time, may lead to reduced residual strength under compressive and bending loadings [6–8], as well as reductions in damage resistance and tolerance [9].

Traditionally, a sandwich structure is made of two thin, stiff faces and a thick, lightweight core. When subjected to external loadings, the facesheets improve the overall stiffness and resistance of the sandwich structure, while the core absorbs most of the energy through plastic deformation. Facesheets are usually made of metal sheets or fiber-reinforced composites [10–12]. Common core configurations include cellular structures such as metal or polymer foams [13–15], graded or auxetic honeycombs [16,17], tetrahedral or pyramidal lattices [18,19] and trapezoidal or sinusoidal corrugated cores [20,21]. As the main component in energy absorption, the core has a significant influence on the global behavior of the

sandwich structure and thus, extensive investigations have been carried out to improve its mechanical properties.

Sun et al. [22] analyzed, through both experimental and numerical methods, the influence of facesheet and core thickness, as well as honeycomb cell size and wall thickness, upon the behavior of sandwich panels with honeycomb core under impact loadings. They found that the core thickness barely affects the failure mechanism, while an increase in facesheet thickness substantially improved perforation resistance and energy absorption capacity. The same group of researchers investigated the dynamic response of homogeneous and stepwise-graded aluminum foam cores subjected to low-velocity impact. They found that the density gradient of graded foam significantly influences the damage mode of the upper facesheet. Additionally, they discovered that the efficiency of sandwich panels can be improved by increasing the front-to-back thickness ratio while keeping the total thickness the same [23]. The temperature effect on the deformation and failure behavior of composite sandwich panels with polymeric foam cores under low-velocity impact was investigated by Yang et al. [15]. Using ultrasonic testing and high-speed cameras, they showed that elevated temperature enhanced the penetration rate and indentation depth, affecting the out-of-plane properties. Mat Daud et al. [24] performed a parametric analysis to investigate the influence of integrating smart materials into composite sandwich structures upon their energy absorption capabilities. They concluded that adding shear-thickening fluids into the core significantly enhanced the energy absorption capacity of the sandwich panel. An increase in energy absorption was observed when incorporating smart materials into facesheets, but only at low energy levels.

Among cellular cores, auxetic structures with a negative effective Poisson's ratio have gained a lot of attention in recent studies as, in addition to enhanced impact resistance and shear toughness [25], they present other improved mechanical properties such as robustness and durability [26], higher energy absorption [27] and vibro-acoustic performances [28].

For several years, additive manufacturing (AM), also known as 3D printing or rapid prototyping, has been imposed as a rather new fabrication technology that uses a 3D computer-designed geometrical model to add material layer by layer, in order to create, with satisfactory geometric accuracy and less waste, objects with sophisticated 3D architectural configurations. Extensive reviews provide significant insight into potential engineering applications and future challenges [29,30]. AM offers greater flexibility in designing innovative structures, allowing materials to be optimally positioned to improve or customize their mechanical properties.

In a recent comprehensive review, Wu et al. [31] presented the advancements in additive manufacturing, focusing on the mechanical properties of materials and structures, particularly for energy absorption usage. They also presented a range of lightweight AM materials and structures, highlighting their mechanical and energy absorption characteristics. The review also covered design optimization methods, such as parametric, topology and nondeterministic optimization, that take into consideration the uncertainties resulting from the fabrication process. Moreover, techniques based on data-driven approaches and machine learning were highlighted for their substantial potential in managing process-property relationships and enabling real-time monitoring during fabrication.

Sarvestani et al. [32] used a semi-analytical and numerical approach and conducted experimental impact tests to assess the mechanical behavior and energy absorption capabilities of sandwich panels with hexagonal, rectangular and auxetic core topologies under low-velocity impact. Their results showed that the auxetic sandwich panel has a higher energy absorption capacity and minimum transferred impact forces.

Wang et al. [33] showed through theoretical, numerical and experimental analysis that the concave angle and graded design of a novel auxetic honeycomb can improve its energy absorption capabilities. In their work, Li et al. [34] demonstrated through a multi-scale modeling approach and a nonlinear analysis that sandwich plates with graphene-reinforced composite facesheets and functionally graded auxetic 3D lattice cores have superior low-velocity impact resistance when compared to non-auxetic sandwich structures. Lu et al. [35]

investigated the out-of-plane failure behavior under dynamic loadings of different auxetic chiral structures regarding plateau stress, peak stress and energy absorption efficiency. They found that anti-tetrachiral structures have superior energy absorption capacity than hexachiral structures due to higher recorded values of plateau stress. The experimental investigations of Wei et al. [36] upon auxetic star honeycombs with different cell angles showed that the cell wall angle can improve the energy absorption capacity of the structure but has no clear effect on the deformation mode. Also, the numerical results indicated that an increase in energy absorption can be achieved by reducing the orthogonal array ratio and length of the ligament. In their work, Guo et al. [37] proposed three new 3D double arrow-head plate lattice auxetic structures and investigated their quasi-static fracture and low-velocity impact response. The results indicated that the proposed structures present a stiffer auxetic behavior and better impact resistance than other lattice structures with low densities. Through both experimental and numerical analysis of low-velocity impact, Özen et al. [38] investigated the mechanical response under three different impact energies of woven carbon-fiber-reinforced plastic (CFRP) facesheet sandwich panels with thermoplastic Acrylonitrile Butadiene Styrene (ABS) honeycomb and re-entrant cores.

This paper completes the studies of the mechanical behavior and energy absorption capabilities of sandwich panels with honeycomb and re-entrant core structures subjected to low-velocity impact. Using the fused deposition modeling (FDM) technique and polylactic acid (PLA), three sandwich panels with different core topologies were fabricated: regular hexagonal, re-entrant at 0 degrees with cells in horizontal position and re-entrant at 90 degrees with cells in vertical position. Each sandwich panel was printed as a whole, meaning that the connection between the core and both facesheets was made directly during the printing process, with no adhesive being used. All three cores have the same cell wall thickness and relative density. The cell design parameters for each topology, the fabrication procedure of the sandwich panels and the PLA mechanical properties established through testing are also presented. This paper describes the setup for the experimental testing and the finite element model established to perform numerical simulations for low-velocity impact testing at impact energies of 10 J and 15 J. Experimental and numerical results are further presented, showing the response of re-entrant and regular honeycombs loaded in impact. At the end of this paper, Section 5 summarizes the outcomes.

## 2. Materials and Methods

### *2.1. Unit Cell Design*

Two types of unit cells are used to create the configuration of the sandwich panel core: hexagonal and re-entrant. The geometric configurations are presented in Figure 1, characterized by the following primary parameters: $t$—cell wall thickness, $h$—vertical cell height, $l$—length of the inclined cell wall and $\theta$—angle between the horizontal line and inclined wall.

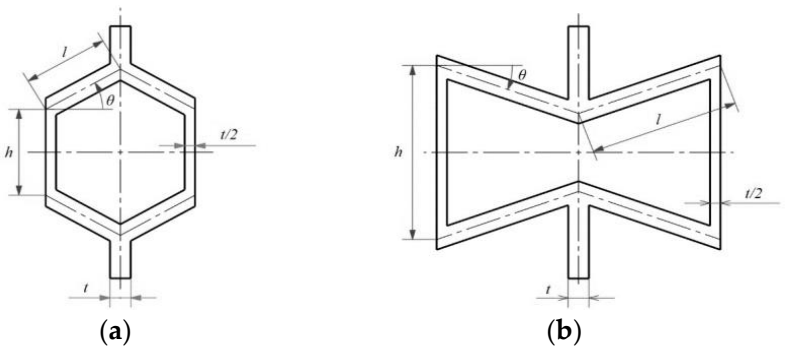


(**a**) (**b**)

**Figure 1.** Geometrical configuration of the unit cells: (**a**) hexagonal and (**b**) re-entrant.

The relative density of the hexagonal unit cell is calculated using Equation (1) and the following values of the cell parameters: $t = 0.8$ mm, $l = 3.343$ mm, $\theta = 30°$ and $h = 3.579$ mm.

$$\frac{\rho^*}{\rho_s} = \frac{2th + 4tl - t^2 tan\theta - 2t^2 tan(\pi/4 - \theta/2)}{2lcos\theta(2h + 2lsin\theta)} \quad (1)$$

The same calculations were made for the re-entrant unit cell but using Equation (2), [39], and the following values of the cell parameters: $t = 0.8$ mm, $l = 5.676$ mm, $\theta = -20°$ and $h = 7.191$ mm.

$$\frac{\rho^*}{\rho_s} = \frac{t/l(h/l + 2)}{2cos\theta(h/l + sin\theta)} \quad (2)$$

The established dimensions are theoretical, as they result from the unit cell design and cannot be achieved by using FDM printing. The relative densities of the regular hexagonal and re-entrant cells were calculated as 25%.

### 2.2. Fabrication of Sandwich Panels

The considered square sandwich panels were fabricated with the Ultimaker S5 Pro Bundle printer and two types of 2.85 mm filaments: Ultimaker PLA Green 1608 and Ultimaker TPU 95A Blue 1334 (Ultimaker, Utrecht, The Netherlands), using the FDM printing technique. The STL files needed to generate the printing files were imported directly from the CAD model created using CATIA V5 software. The resulting configurations of the sandwich panels are presented in Figure 2. All panels have the following dimensions: equal length with a width of 110 mm, total height of 31 mm, the thickness of each facesheet of around 5 mm and cell wall thickness of about 0.8 mm; to be more precise for PS1 5.08 mm and 0.83 mm, for PS2 5.14 mm and 0.84 mm, and for PS3 5.12 mm and 0.87 mm.

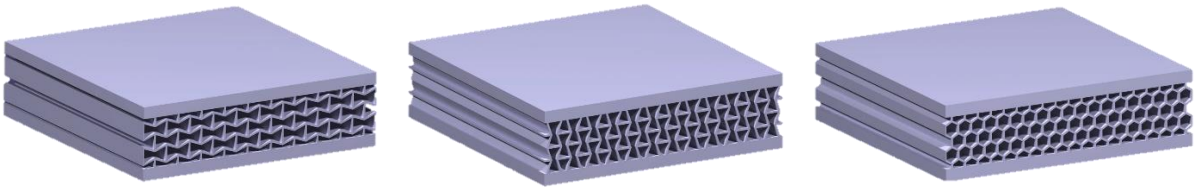

(**a**) (**b**) (**c**)

**Figure 2.** Configuration of sandwich panels with (**a**) PS1 (0 degree re-entrant), (**b**) PS2 (90 degree re-entrant) and (**c**) PS3 (regular hexagonal) cores.

An extruder type AA 0.4 was used to print all panels with the CURA software version 5.8 by choosing the same printing parameters: infill density 100%, number of contours 3, layer thickness 0.2 mm, raster angle ±45°, bed temperature 60 °C, printing temperature 205 °C, printing speed 70 mm/s. Table 1 shows, for each type of sandwich panel, the time of printing and the quantity of PLA used.

**Table 1.** Time of printing and quantity of PLA used for each sandwich panel.

| Sandwich Panel | Time of Printing | Used Quantity [g] |
|---|---|---|
| PS1 (0 degrees re-entrant) | 17 h 12 min | 221 |
| PS2 (90 degrees re-entrant) | 16 h 59 min | 223 |
| PS3 (regular honeycomb) | 16 h 48 min | 220 |

### 2.3. Traction Tests

The mechanical properties of PLA were obtained through standard tensile tests at a testing speed of 1.5 mm/min according to ASTM D638-22 [40]. When printing the tensile specimens, different thicknesses of the printing layer were used to establish the best printing-quality-to-time ratio. The values ranged between 0.06 mm to 0.3 mm according to the printing equipment's performance. Traction tests were performed on an INSTRON 68TM-50 with a force cell of 50 kN and using an INSTRON 2630-100 extensometer.

The dimensions for specimen type 1 are given in Figure 3a, and five tested specimens made from Ultimaker PLA Green 1608 (Ultimaker, Utrecht, The Netherlands) with a layer thickness of 0.2 mm are shown in Figure 3b.

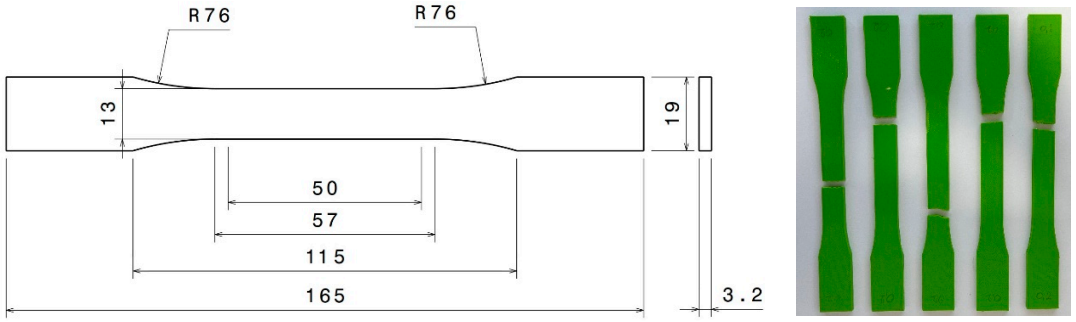


**Figure 3.** Tensile specimens: (**a**) dimensions in mm and (**b**) tested specimens printed with a layer thickness of 0.2 mm.

Different printing layer thicknesses were adopted: 0.06 mm, 0.1 mm, 0.15 mm, 0.2 mm and 0.3 mm. The layers were consecutively oriented at +45 degrees and −45 degrees with respect to the loading direction. The time needed to print five specimens with a layer thickness of 0.2 mm is 3 h and 28 min (as compared to 9 h and 46 min for the layer thickness of 0.1 mm and 16 h and 13 min for the layer thickness of 0.06 mm) by using 52 g and an equivalent of 6.52 m of filament. Obviously, the layer thickness influences the mechanical properties of the PLA specimens, as seen in Figure 4. Before testing, the specimens were kept for 7 days in the laboratory at a temperature of 20–23 °C to allow the complete curing of the material.

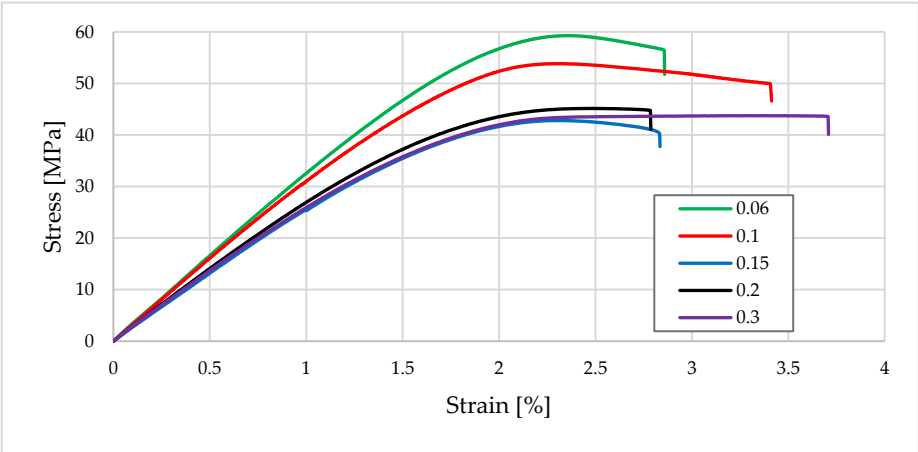


**Figure 4.** Average tensile engineering stress–strain curves for specimens printed with different layer thicknesses.

The resulting average engineering stress–strain curves (five tests for each layer thickness were performed) are presented in Figure 4. Eventually, a layer thickness of 0.2 mm was chosen for printing the sandwich panels as a good compromise between the time needed for printing the specimen, which becomes prohibitive for layer thicknesses of 0.06 mm and 0.1 mm, and its stiffness.

However, the increase in resulting strength, from about 45 MPa to less than 60 MPa, does not justify the significant time consumption, as elongation at failure remains about the same, around 2.8–3.5%.

Digital image correlation (DIC) traction tests were performed with a Dantec Dynamic Q-400 MicroDIC (µDIC) system, with cameras of 5 megapixels and ISTRA4D 4.6 software. The dimensions of the facets were 55 × 55 pixels, and to ensure a good superposition of the facets, the distance between their middles was 53 pixels.

Considering the already obtained results, only two traction tests for layer thicknesses of 0.15 mm, 0.2 mm and 0.3 mm were conducted, which is relevant to our results (Figure 5a). The local values of the principal strain immediately before the failure of the specimens were around 45–50 strain/mstrain, as indicated in Figure 5b for 0.2 mm layer thickness, which is 4.5–5.0%.

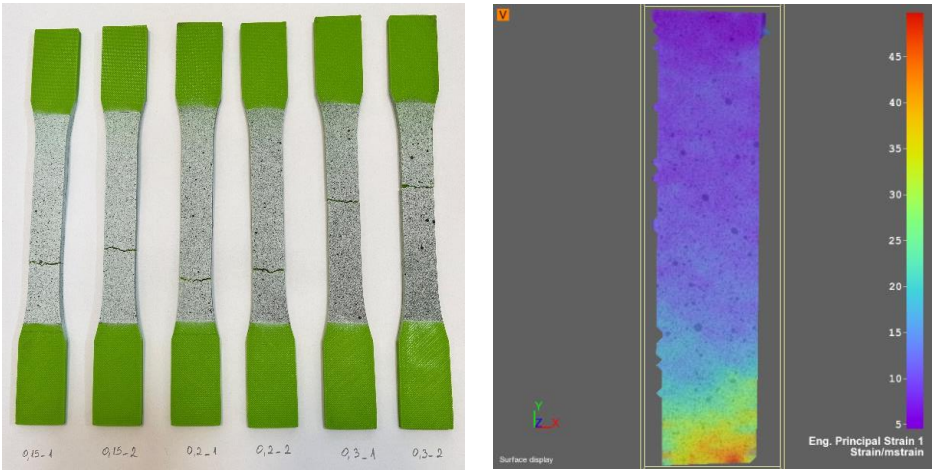


(**a**) (**b**)

**Figure 5.** Traction DIC analysis: (**a**) 0.15 mm, 0.2 mm and 0.3 mm layer thickness tested specimens and (**b**) principal strain at failure for 0.2 mm layer thickness.

### *2.4. Compression Tests*

Cubic specimens of 20 × 20 × 20 mm were tested in compression at the same 1.5 mm/min crosshead speed on the same testing machine as for traction. For each layer thickness, five specimens were tested. Figure 6 presents the average force-displacement curves obtained for all layer thicknesses.

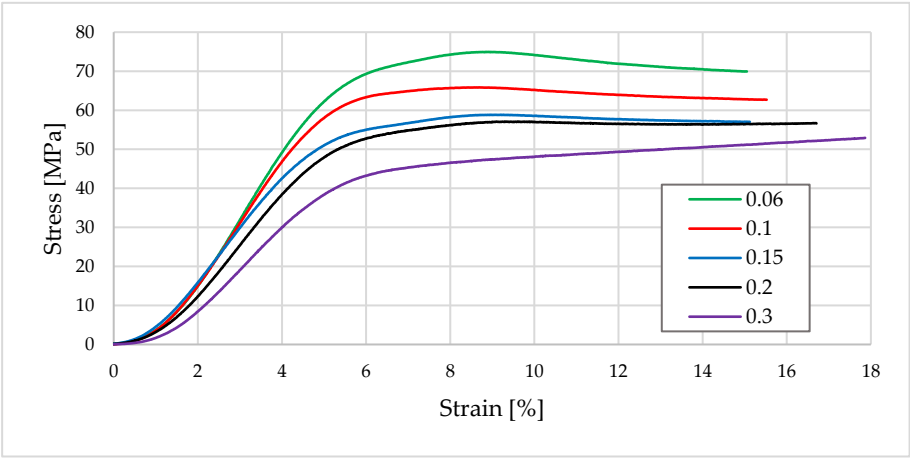


**Figure 6.** Average compression force-displacement curves for specimens printed with different layer thicknesses.

Compression tests indicate that, as for traction, the specimens with layer thicknesses of 0.06 mm and 0.1 mm give the highest values of the compression force; the lowest value

is for a layer thickness of 0.3 mm, the force-displacement curve being now further away from the one obtained for 0.2 mm layer thickness. This trend is in contradiction with the curve obtained for traction, which was 0.3 mm in the vicinity of the 0.2 mm curve.

To better understand the failure mechanisms in compression, the DIC method (Figure 7a) was also used to obtain the maximum principal compressive strains. Considering the local effects at the contact between the compression platens and the specimen, Figure 7b shows that principal strain variation follows shear bands of failure at about 80–100 strain/mstrain (8–10%), having an average value twice that which resulted for traction. Clearly, the Ultimaker PLA demonstrates fragile behavior.

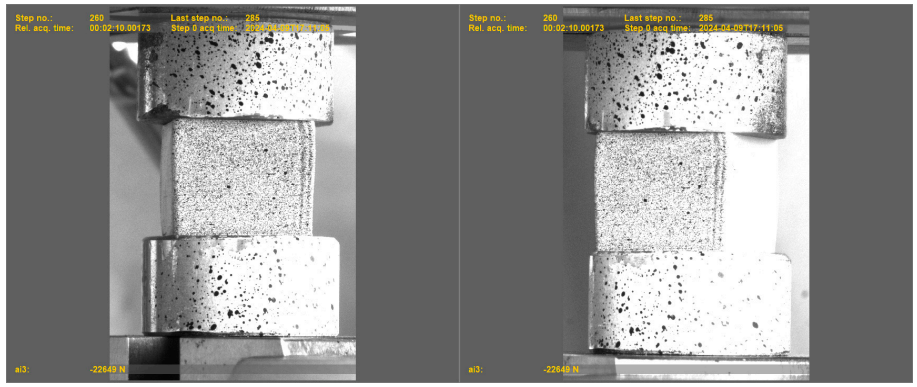


(**a**)

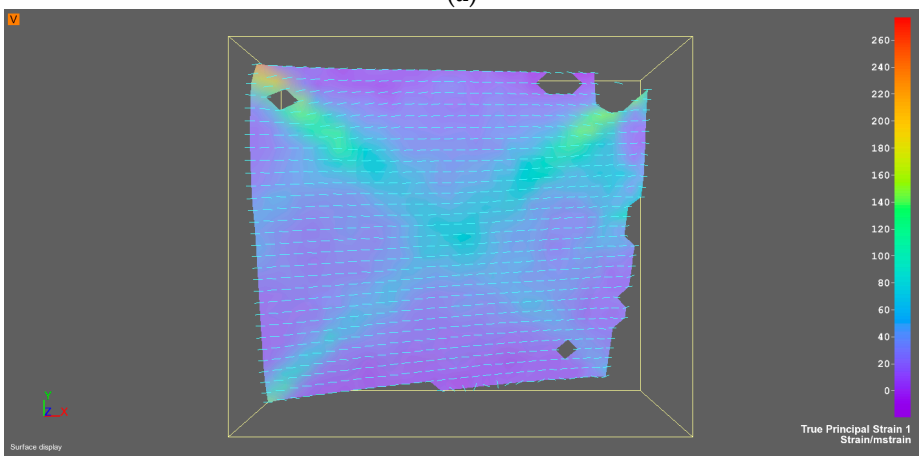


(**b**)

**Figure 7.** Compression DIC test for a specimen with 0.2 mm layer thickness: (**a**) positioning of the specimen as observed with the two cameras and (**b**) principal strain variation at the end of the test.

## 3. Low Velocity Impact Testing

### *3.1. Experimental Procedure*

Low-velocity impact tests have been carried out on the printed sandwich panels using the drop test machine INSTRON 9340. An impactor with a hemispherical striker tup insert of 20 mm diameter and a total mass of 3.233 kg are used. The release height of the impactor is set to obtain the desired impact energies of 10 and 15 J. These energies were chosen after preliminary testing, as we wanted to obtain a dominantly elastic response of the sandwich panels, but at the same time to observe the failure mechanisms of the cell walls. Data acquisition is conducted by using an INSTRON CEAST DAS-64K system at a frequency of 1000 kHz.

For each tested sandwich panel PS1, PS2 and PS3 at an impact energy of 10 J and 15 J, the symbolic notation is used: for example, PS1_15 means sandwich panel with re-entrant 0 degrees core tested at 15 J impact energy.

Special attention was given to establishing the force with which the sandwich panel is fixed between the upper and lower steel plates. The upper plate fixes the panel through a pneumatic system towards the lower plate, for which the vertical position was adjusted with a screw-nut mechanism (Figure 8a). As such, the relative position of the panel influences the boundary experimental conditions is to be properly considered later in the numerical simulations. Therefore, it is important to know the force with which the sandwich panel is pressed in between the upper and lower fixing plates.

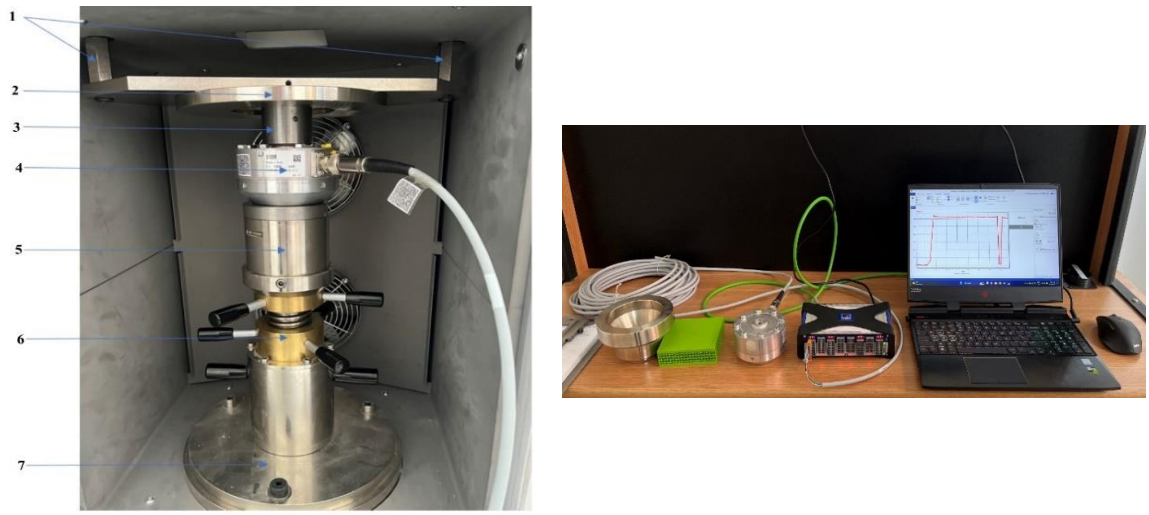


(**a**) (**b**)

**Figure 8.** Measurement setup of the force pressing the sandwich panel: (**a**) load fixture and (**b**) measuring system of the force.

Figure 8a shows the gripping system of the sandwich panel and the measuring system of the force to be applied by the upper plate that holds the panel. It shows (1) the two pneumatic cylinders that, through a plate, are pressing the upper plate (2), which is in contact with the top facesheet of the sandwich panel. The HBK force transducer (4) is pushed downwards through an intermediate cylindrical nut (3), which is used only in this setup to compensate for the gap. The force transducer leans on a lower support (5), which, in turn, is fixed to the screw-type mechanics (6). With (7) is notated the base fixture of the whole assembly with which the sandwich panel is fixed. In reality, instead of the nut and force transducer, a lower plate is placed, as seen in Figure 8b at the left of the printed sandwich panel.

The measuring system of the force (Figure 8b) comprises a Quantumx MX1615B module (HBK, Germany) with 16 channels, a force transducer U10M, a laptop with CatmanEasy software 5.6.1 and connecting cables. The force that presses the sandwich was measured by adjusting the screw-type mechanism (6) to have a tight fixture while avoiding any damage produced to the panel. The clamping force was measured at around 500 N.

### *3.2. Numerical Simulations*

The numerical simulations were carried out using the commercial finite element code Ansys Workbench. The impact testing setup designed in CATIA V5 software consists of an impactor, clamping plate, sandwich panel and support. Considering the two symmetry planes, only a quarter of the impact assembly was modeled. Meshing was performed using Solid 187 tetrahedral elements, with an adequate refinement near the impact area and dedicated contact elements type Conta 174 and Target 170, in order to provide accurate results in this region (Figure 9). The total number of nodes is 110,678, of contact elements 11,600 and of solid elements 62,402.

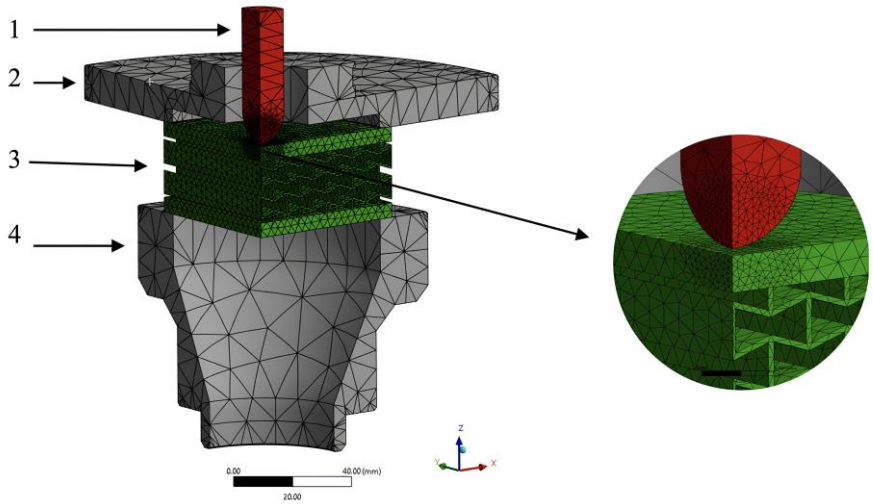


**Figure 9.** Finite element model of the impact testing setup: 1—impactor, 2—clamping plate, 3—sandwich panel and 4—support.

The impactor (1), clamping plate (2) and support (3) were modeled using the Structural Steel material model. For the PLA sandwich panel, the Multilinear Isotropic Hardening material model was used. This material model allows the consideration of a true stress versus plastic strain curve to describe an elastoplastic behavior of the material. Using the stress–strain curve presented in Figure 4, the plastic strain values are calculated as

$$\bar{\varepsilon}^p = \varepsilon_{total}^T - \frac{\sigma^T}{E} \tag{3}$$

where $\bar{\varepsilon}^p$ is the effective plastic strain, $\varepsilon_{total}^T$ is the total true strain and $\sigma^T$ is the true stress [41].

The main average mechanical properties established experimentally for the tested PLA were as follows: Young's modulus 2870 MPa, Poisson's ratio 0.34, ultimate stress for traction 45 MPa, ultimate stress for compression 56 MPa and failure strain in traction 5%. The density is 1250 kg/m$^3$. The ultimate stress used in the numerical analysis was 56 MPa.

All degrees of freedom for the support are blocked. For the clamping plate, the vertical movements are blocked, and the other two directions are left free, while the impactor can only move along the vertical direction. Initial velocities of 2.5 m/s were considered for the impactor, corresponding to an impact energy of 10 J for the total mass of 3.233 kg of the impactor. Frictionless contact between the clamping plate and upper facesheet, support and bottom facesheet, and impactor and sandwich panel was used. The numerical model was validated for 10 J impact energy and was also used for 15 J impact energy.

## 4. Impact Testing Results

### *4.1. Experimental Results*

In order to analyze the behavior of the 3D-printed sandwich panels following the impact tests at low speeds, the variations of the impact force were graphically represented according to the travel time of the impactor. Figure 10 presents a comparison between the three types of panels. It can be seen that the honeycomb core panel PS3_10 records the highest values for the impact force but much faster unloading. The 90 degrees re-entrant core panel (PS2_10) shows a similar behavior during the first portion of loading until the maximum force is reached, after which the upper facesheet fails, followed by the core failure. The panel with 0 degrees re-entrant core (PS1_10) records the lowest impact force values but much slower unloading due to the large deformation of the core walls.

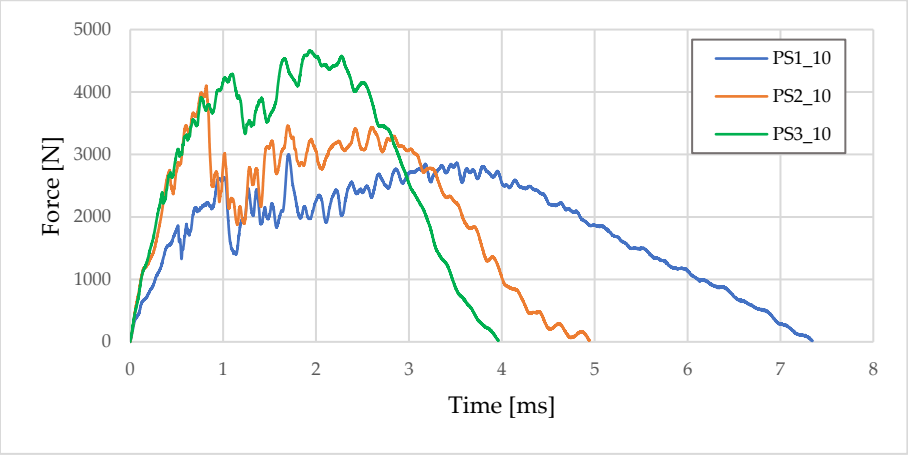


**Figure 10.** Force–time responses of sandwich panels under 10 J impact loading.

An approximately linear increase can be seen for the PS1_10 over the first portion, and at 1 ms impact time, a peak of 2632.74 N is reached for the force. After reaching the first peak, the force suddenly drops below 1500 N due to the damage to the upper face in the impact area; then, a maximum force of 2997.69 N is recorded, followed by a sudden decrease and several oscillations due to the failure of the core walls. It can be seen that the unloading of the sandwich panel is slower than the loading due to the core deforming and absorption of the impact energy. As with the previous panel, a linear increase can be seen in the first part for the PS2_10 panel. After the force registers a maximum of 4102.47 N, there follows a sudden decrease corresponding to the damage of the upper face of the sandwich panel in the impact area. Peaks followed by dips are due to core wall damage. A faster decrease is observed for this panel compared to the PS1_10 panel. As for the previous panels, a linear increase can be seen in the first part for the PS3_10 panel. After the force registers a maximum of 4291.33 N, a plastic deformation of the upper face appears, followed by the failure of the core in the impact zone. A maximum impact force of 4661.96 N is recorded. A much faster unloading is observed for this panel than for the SP1 panel. This demonstrates that the honeycomb core sandwich panel is stiffer.

Figure 11 shows the sandwich panels after the impact tests at an energy of 10 J. The damage of the upper faces in the impact area can be observed, mainly for PS2_10 and PS3_10. The PS1_10 panel with 0 degrees re-entrant core stands out as the top face is less damaged in the impact test compared to the other two types due to the larger deformation of the core.

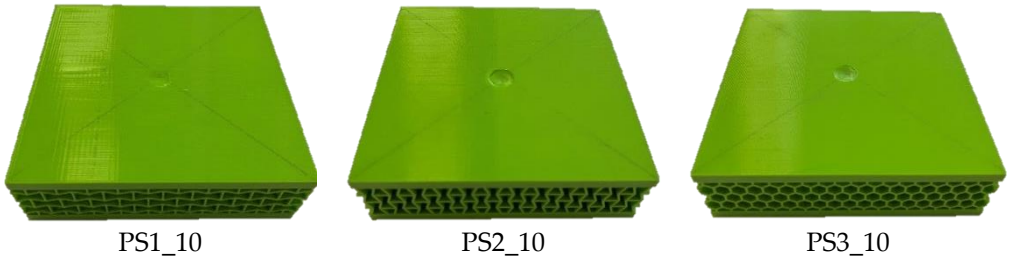


**Figure 11.** Indentation of PLA sandwich panels after 10 J impact tests.

From the impact force variation as a function of impactor displacement (Figure 12) for the specimens tested at an impact energy of 10 J, it can be seen that the PS1_10 records the highest value of 5.28 mm deformation. After unloading, the sandwich panels remain with residual deformations for PS1_10 and PS2_10 of approximately 1.5 mm and for PS3_10 of 2.1 mm.

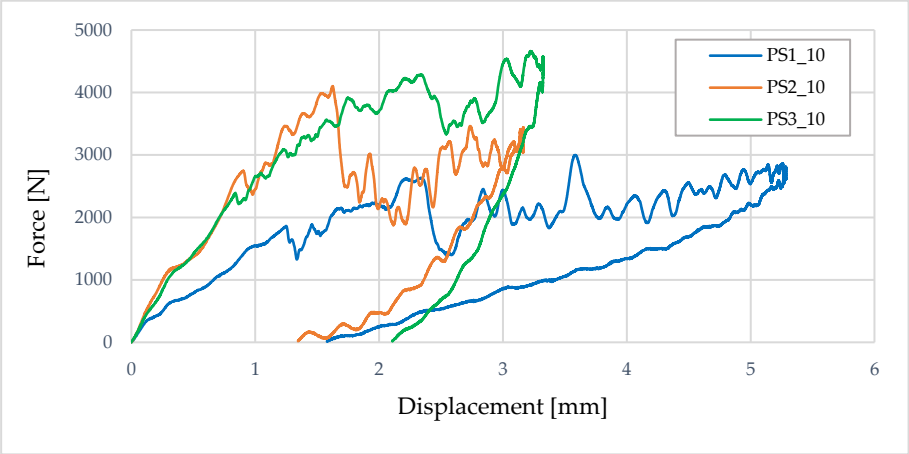


**Figure 12.** Force–displacement responses of sandwich panels under 10 J impact loading.

Figure 13 shows the variation of the impact energy of the sandwich panels as a function of time. The impact energy values were acquired directly from the software used by the test equipment. The PS1_10 panel records the highest value of absorbed energy due to the possibility of deformation of the core walls.

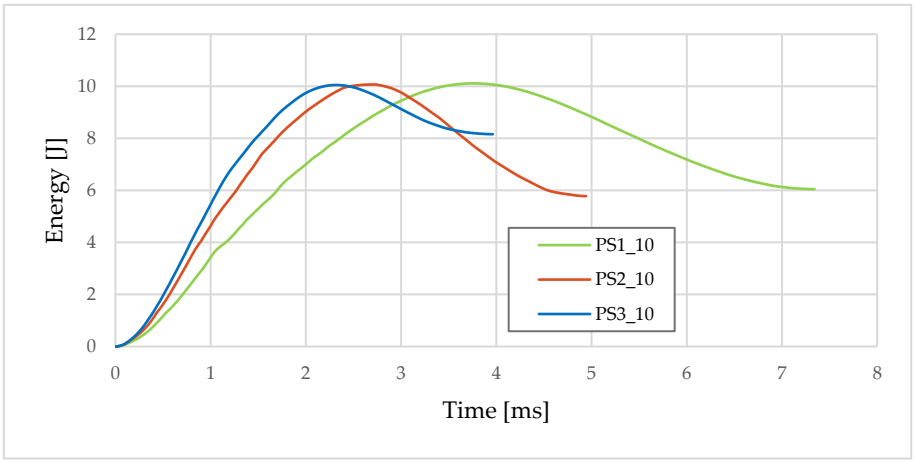


**Figure 13.** Energy–time histories of sandwich panels under 10 J Impact loading.

Based on the energy variation curves as a function of time presented in the figure above, three characteristic quantities can be identified, namely: the impact energy corresponding to the maximum value on the curve, the absorbed energy corresponding to the final value on the curve and the difference between the impact energy and the absorbed energy representing the returned energy.

The comparison between the test results at an impact energy of 15 J is presented in Figure 14. This comparison highlights, again, the very close behavior of the PS2_15 and PS3_15 panels. The PS1_15 panel shows a much slower decrease in the force compared to the other two panels.

Figure 15 presents the variation of force with impactor displacement. The area under these curves represents the total energy absorbed by the panels during the impact tests. The PS1_15 panel shows the highest displacement of 7.2 mm, while the other panels only show 4.75 mm for the PS2_15 and 4.62 mm for the PS3_15 panel.

Figure 16 shows the variation of the impact energy of the sandwich panels as a function of time.

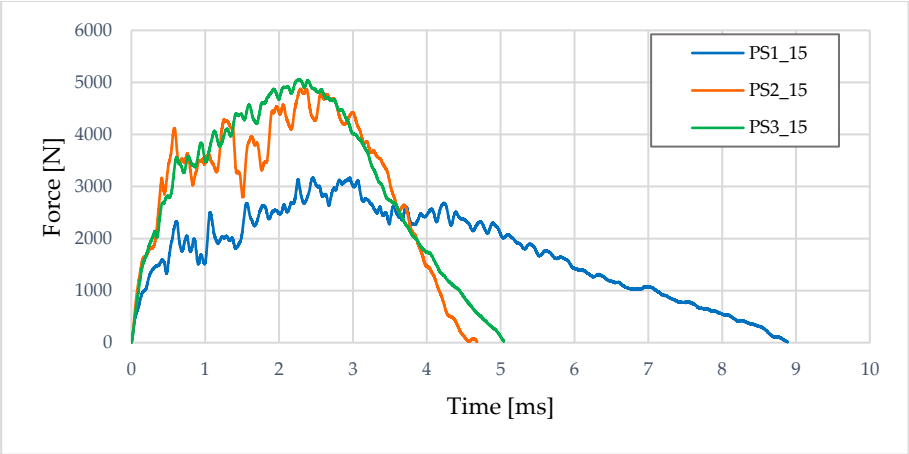


**Figure 14.** Force–time responses of sandwich panels under 15 J impact loading.

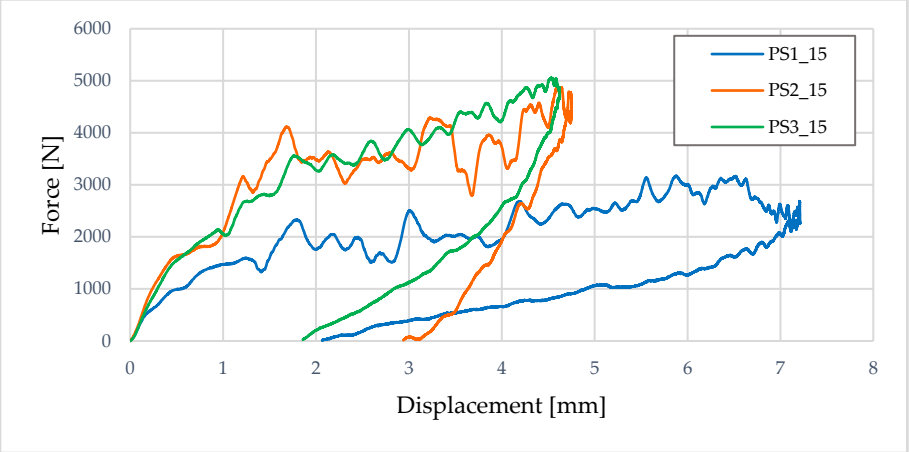


**Figure 15.** Force–displacement responses of sandwich panels under 15 J impact loading.

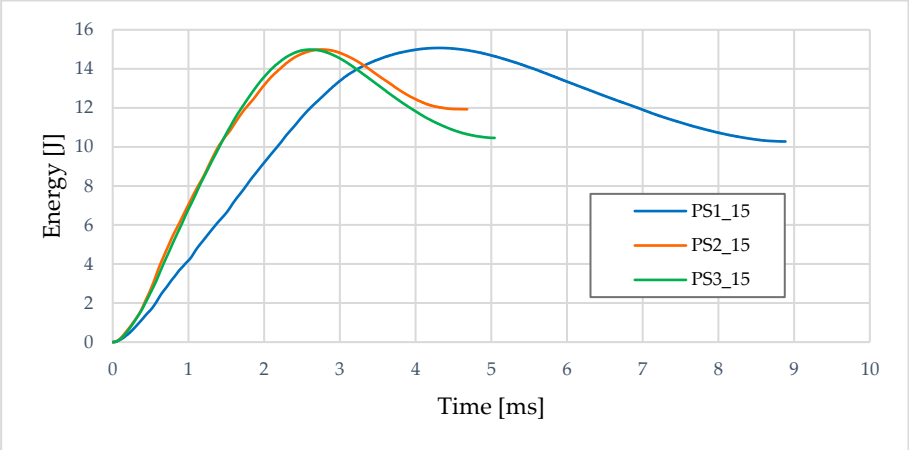


**Figure 16.** Energy–time histories of sandwich panels under 15 J Impact loading.

All three panels end up recording an impact energy of 15 J at different moments: the PS1_15 panel at 4.2 ms, the PS2_15 at 2.7 ms and the PS3_15 at a time of 2.5 ms, showing close values for the last two panels.

The top faces of the impacted sandwich panels are presented in Figure 17. Panel PS2_15 with 90 degrees re-entrant cells is visibly the most damaged, having, as to be seen further, the highest total absorbed energy and highest normalized absorbed energies.

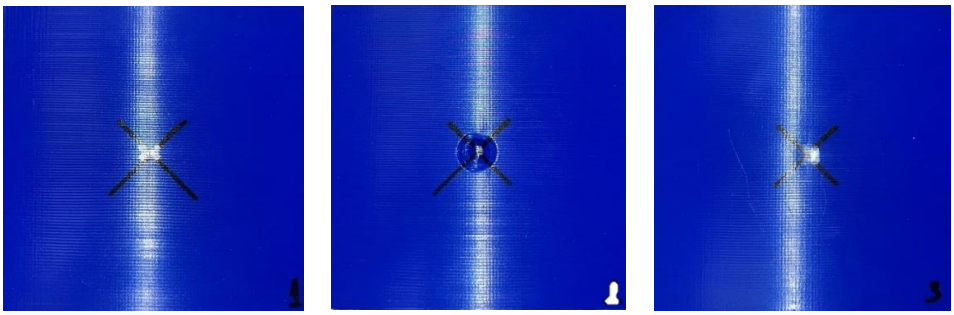


**Figure 17.** PLA sandwich panels after impact tests at 15 J.

In order to easily compare the performance of 3D-printed sandwich panels, Table 2 shows the mass of the tested samples, the maximum force recorded during the impact tests, the average force, the total absorbed energy, the normalized absorbed energy, the specific absorbed energy and the efficiency of the impact force [42–44]. The total absorbed energy ($TAE$) represents the area under the force-displacement curve and can be calculated by integrating the function $F(\delta)$

$$TAE = \int_0^{\delta} F(\delta) d\delta. \tag{4}$$

**Table 2.** Energy performance assessment parameters.

| Sandwich Panel | Mass [g] | $F_{max}$ [N] | $F_{average}$ [N} | $TAE$ [J] | $NAE$ [-] | $SAE$ [J/kg] | $CFE$ [-] |
|---|---|---|---|---|---|---|---|
| PS1_10 | 222.55 | 2997.69 | 1811.63 | 6.03 | 0.603 | 27.10 | 0.60 |
| PS2_10 | 222.16 | 4102.47 | 2194.75 | 5.76 | 0.576 | 25.93 | 0.53 |
| PS3_10 | 218.23 | 4661.96 | 2927.36 | 8.14 | 0.814 | 37.30 | 0.63 |
| PS1_15 | 219.67 | 3172.35 | 1749.86 | 10.27 | 0.685 | 46.75 | 0.55 |
| PS2_15 | 219.20 | 4873.55 | 3065.67 | 11.90 | 0.793 | 54.29 | 0.63 |
| PS3_15 | 217.48 | 5052.47 | 3035.54 | 10.44 | 0.696 | 48.05 | 0.60 |

In order to be able to compare the absorption capacity of different structures, it is usually preferred to use the normalized absorbed energy value ($NAE$), which is defined as the ratio of the total absorbed energy ($TAE$) to the impact energy ($IE$):

$$NAE = \frac{TAE}{IE}. \tag{5}$$

The specific absorbed energy ($SAE$) is the ratio between the total absorbed energy and the mass of the sandwich panel:

$$SAE = \frac{TAE}{m_{panel}}. \tag{6}$$

A high value of the $SAE$ parameter indicates that the structure has an increased energy absorption capacity and a reduced weight. In engineering applications, another index used to compare the energy absorption capabilities of structures is the crush force efficiency ($CFE$), which is defined by the relationship:

$$CFE = \frac{F_{average}}{F_{max}}, \tag{7}$$

where $F_{average}$ represents the average impact force, and it is calculated based on the results recorded from the impact tests, being an arithmetic mean (the sum of the values recorded for the force in relation to the number of records) and $F_{max}$ represents the maximum force from the force-displacement graph: $F_{max} = max|F(\delta)|$.

### 4.2. Experimental and Numerical Results

The following graphs present the results of the experimental and numerical analyses for the impact on PS1_10 (Figure 18) and PS1_15 (Figure 19).

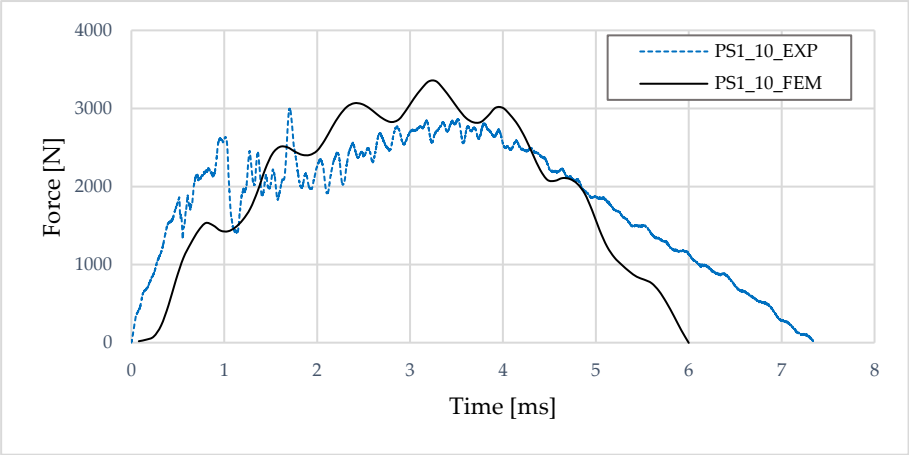


**Figure 18.** Comparison between experimental results and numerical analysis for panel PS1_10.

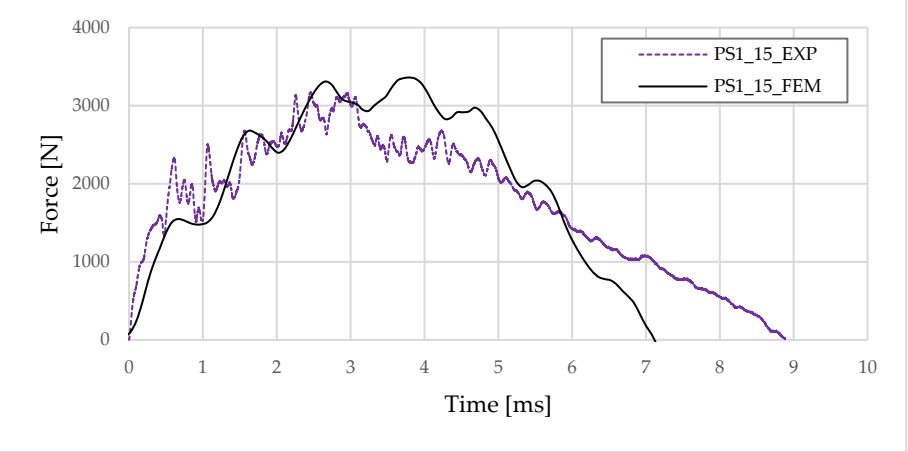


**Figure 19.** Comparison between experimental results and numerical analysis for panel PS1_15.

For both impact energies, the experimental and numerical variations of the contact impact force in time are similar, with higher values being obtained numerically. The variation of force shows refined fluctuations for the experimental testing due to complicated local phenomena, which cannot be captured in the numerical model. The duration of impact is shorter in the numerical analysis, at about 1.5–2 ms.

Figure 20 presents the von Mises equivalent stresses for panel PS1 at 10 J impact energy. The maximum recorded value is about 56 MPa. Figure 21 shows the distribution of the von Mises equivalent stresses for panel PS1 at 15 J impact of energy having about the same maximum value. The equivalent stress distributions can be seen both in the upper face and in the core. The upper face reaches its maximum values in the impact zone and distributes towards the core.

At 15 J impact energy (Figure 21), the upper face deforms more, with 7.2 mm compared to 5.28 mm for 10 J, and the core starts to absorb more energy from the upper face and transmits it over its entire core cells surface, not only in the impact area. The walls have lost stability and show the appearance of local buckling.

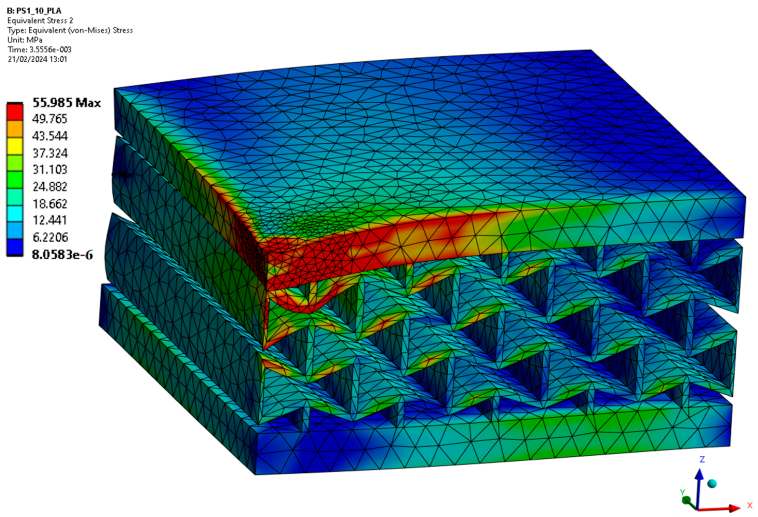


**Figure 20.** The equivalent von Mises stresses for the panel PS1_10.

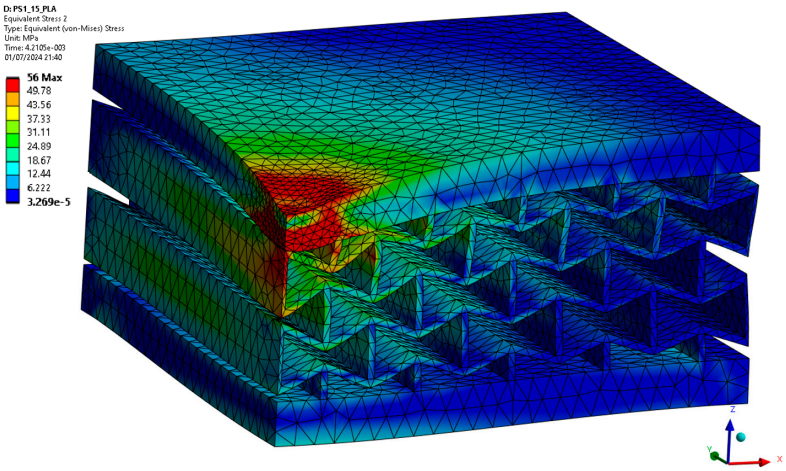


**Figure 21.** The equivalent von Mises stresses for the panel PS1_15.

For PS2_10 (Figure 22), the maximum force recorded for the experimental test is 4103 N, and, in the case of the numerical simulation, the maximum force is 4430 N. For this type of panel, larger differences can be observed between the experimental test and the numerical simulation. In the case of the experimental test, when the maximum force is reached, the upper face fails, and the force drops suddenly from 4102 N to 2500 N. In the case of the numerical simulation, the force shows a decrease after reaching the maximum value, but not as significant. For the PS2_15 impact (Figure 23), the general trend in the force variation is about the same experimentally and numerically, with no sudden drop of force in the experimental testing. The panels PS1 and PS2 have the same relative density; the only difference is the orientation of the cells that form the core.

In the case of the PS2_15 panel, the most loaded row of cells is the one near the impact zone, and the other rows of cells that make up the core are almost completely unloaded. This aspect can be seen in Figure 24.

During the experimental tests at an impact energy of 15 J the upper face yielded exactly in the areas where the maximum stresses were reached. The maximum force recorded for the experimental test is 4873 N, and for the numerical simulation, a maximum force of 5545 N was reached. The recording time of the impact force for the experimental test is 4.58 ms, and for the numerical simulation, it is 3.96 ms.

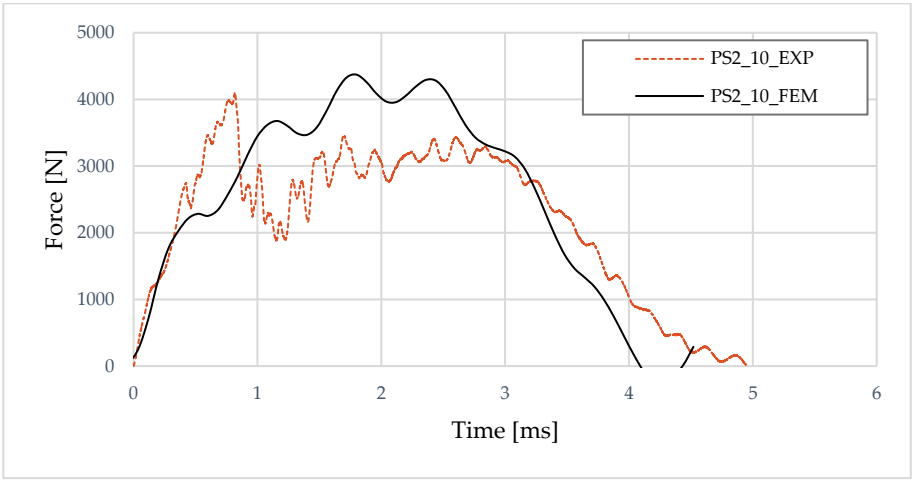


**Figure 22.** Comparison between experimental results and numerical analysis for panel PS2_10.

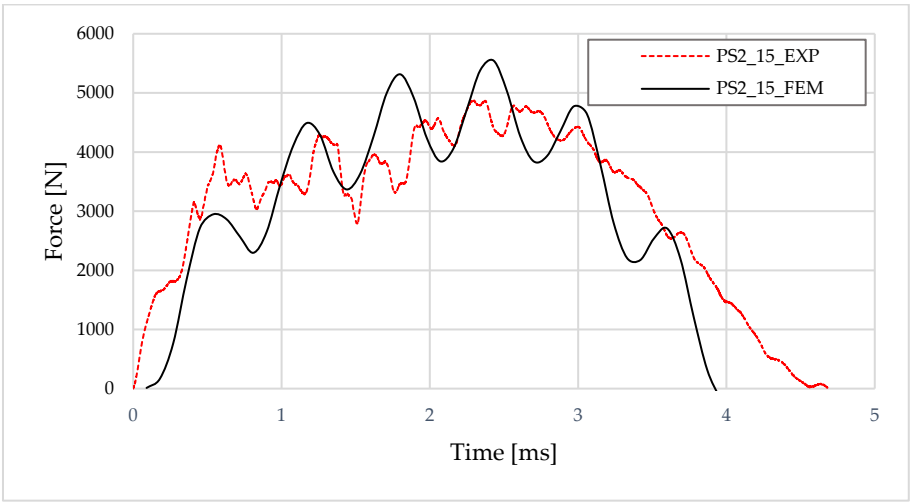


**Figure 23.** Comparison between experimental results and numerical analysis for panel PS2_15.

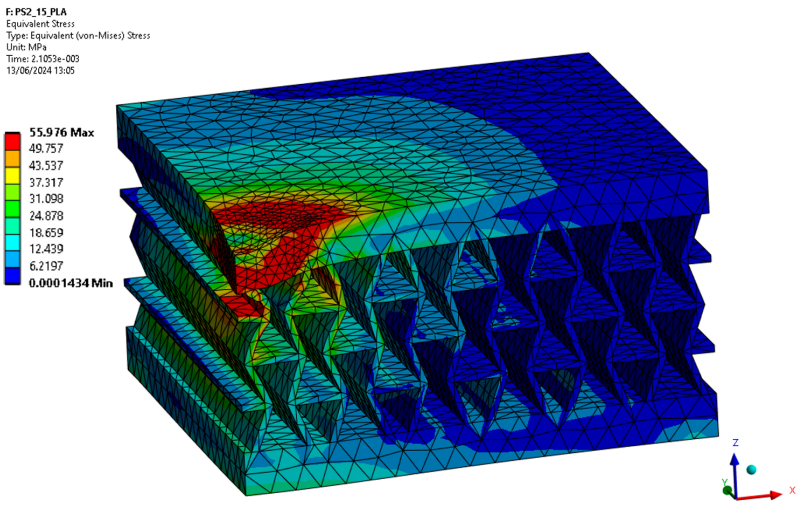


**Figure 24.** The equivalent von Mises stresses for the panel PS2_15.

Finally, for PS3_10 (Figure 25) and PS3_15 (Figure 26), we obtain, in fact, the highest resemblance between the experimental and numerical contact force–impact time variations.

The honeycomb cells are more stable locally during impact than those of the re-entrant cells, especially compared to the ones at 0 degrees, which show a very complicated force variation that cannot be reproduced numerically. As before, the maximum force obtained from numerical simulations has higher values than the one obtained experimentally for both impact energies, and the simulated time of impact is a little bit shorter. The maximum force recorded for the experimental test is 4662 N, and for the numerical simulation is 5270 N. In reality, the sandwich panel cannot be tightly fixed between the two steel plates (small oscillations will appear), and it is impossible to model numerically the real boundary conditions for contact.

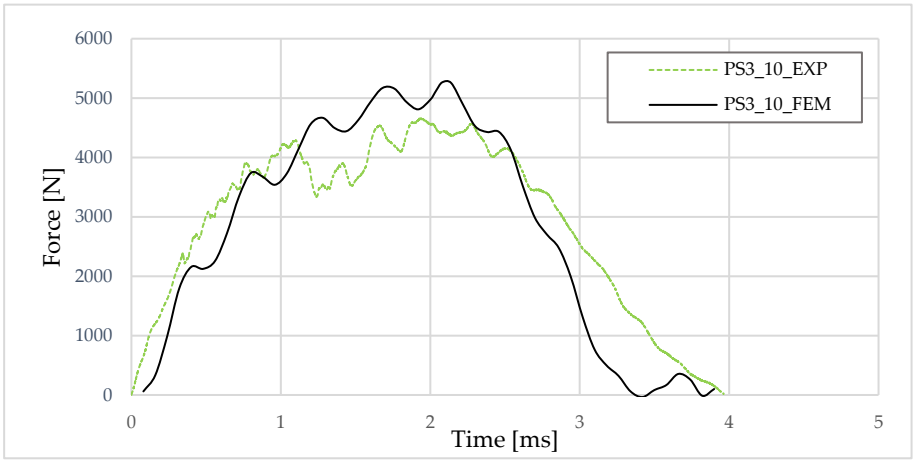


**Figure 25.** Comparison between experimental results and numerical analysis for panel PS3_10.

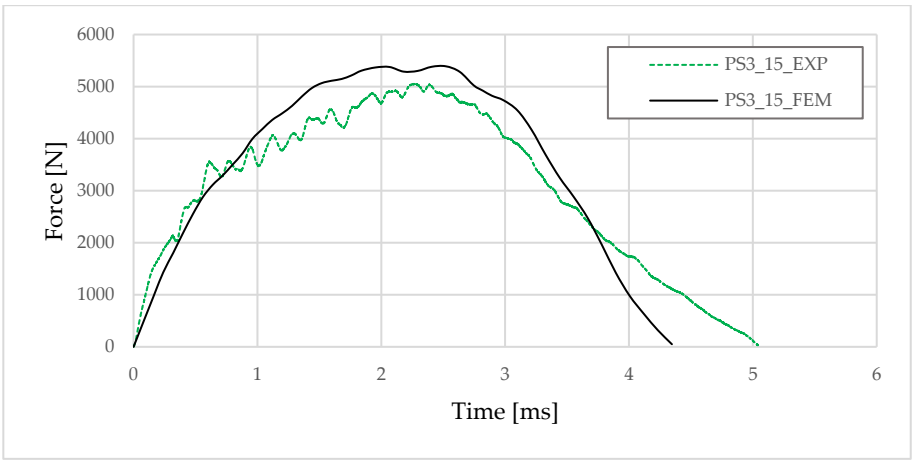


**Figure 26.** Comparison between experimental results and numerical analysis for panel PS3_15.

Figure 27 presents the von Mises equivalent stress variation for panel PS3 at 15 J impact energy. The areas highlighted in red are where the maximum equivalent stress is equal to the yield stress of the material. The walls of the core cells do not reach the maximum yield stress of the material, with the exception of the inclined walls near the impact zone.

Table 3 presents a comparison of impact energy of 15 J between the results obtained from experimental tests and the results obtained from numerical simulations for the maximum force of impact, average impact force and total absorbed energy. The relative errors between the experimental values and those obtained by numerical simulation are also calculated.

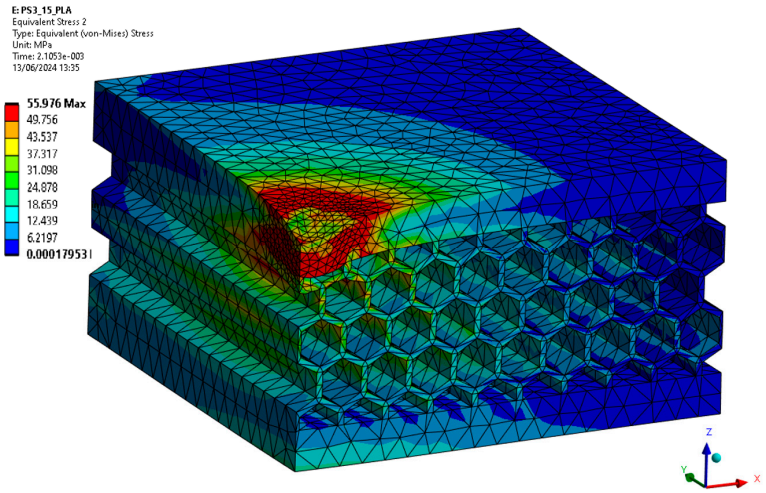


**Figure 27.** The equivalent von Mises stresses for the panel PS3_15.

**Table 3.** Maximum force values, average force values, total absorbed energy values and relative errors between experimental tests and numerical analysis for an impact energy of 15 J.

| Sandwich Panel | $F_{max}$ [N] | | Relative Error [%] | $F_{average}$ [N] | | Relative Error [%] | *TAE* [J] | | Relative Error [%] |
|---|---|---|---|---|---|---|---|---|---|
| | Exp | Num | | Exp | Num | | Exp | Num | |
| PS1 | 3172 | 3360 | 5.59 | 1750 | 1937 | 9.65 | 10.3 | 9.64 | −6.40 |
| PS2 | 4874 | 5410 | 9.90 | 3066 | 3342 | 8.25 | 11.9 | 10.88 | −8.57 |
| PS3 | 5052 | 5390 | 6.27 | 3036 | 3254 | 6.69 | 10.4 | 11.19 | 7.05 |

Comparing these data results the maximum and average forces determined numerically are greater than the experimental ones with an error of up to 10%. On the other hand, the experimentally established total absorbed energy is greater than the numerical counterpart for both re-entrant structures but lower for the regular honeycomb. However, the differences are acceptable, thus giving confidence that the numerical model can be successfully used for low-velocity impact and low levels of impact energy.

## 5. Conclusions

The impact performance evaluation of PLA 3D-printed sandwich panels with 0 and 90 degree re-entrant cores and regular honeycomb cores at low-velocity impact with energies of 10 J and 15 J (in total, six types of sandwich panels) gives interesting results. When analyzing the total absorbed energy *TAE* and the normalized impact parameters as normalized absorbed energy *NAE*, specific absorbed energy *SAE* and crush force efficiency *CFE*, one also has to observe the behavior of the impacted panels and the damage produced during impact.

The *CFE* normalized parameter always remains between 0.53 and 0.63, showing that the general impact response of all panels remains about the same in terms of average and maximum impact force. The *TAE* and the *SAE* indicate differences in the response of the cores, depending on their geometry, as their mass is not much different—between 217 and 223 g. Panel PS1 0 degree re-entrant is the most compliant, having the highest displacement at impact but much lower stiffness and strength than PS2 and PS3 (Figure 15). On the other hand, its recovery at 15 J impact energy is similar to the PS3 regular honeycomb, both having about 2 mm remanent deformation. The PS2 90 degrees re-entrant panel has similar stiffness and strength as PS3 but a smaller final deformation of 3 mm, leading to a higher experimental *TAE* (Table 3). The PS2_15 panel also has the highest values of *SAE* and *NAE*. However, the upper face of this panel is the most severely damaged (Figure 17) because of its higher rigidity. The PS1 0 degrees re-entrant panel demonstrates more elastic behavior, and although it absorbs 13% less energy than its counterpart, the upper face did not suffer

visible damage. The core walls cracked along the entire height of the panel in the impact area. This type of panel is preferable in engineering applications where it is necessary for the outer surface to remain as intact as possible while absorbing a substantial amount of energy. The 0 degrees re-entrant core is compliant and provides both impact resistance and good energy absorption characteristics. As an application, such a core can be used in the construction of personal protective equipment, where the aim is to minimize the forces transmitted during low-velocity impacts and maximize the total absorbed energy.

Essentially, the honeycomb core sandwich panel remains one of the favorite candidates in impact engineering, but depending on the specific application, the re-entrant core panels can offer more flexibility for 0 degrees or more stiffness for 90 degrees position of the cells.

**Author Contributions:** Conceptualization and supervision, D.M.C.; experimental analysis, A.I.I. and O.A.M.; numerical analysis, A.I.I. and Ș.S.; writing—original draft, A.I.I. and O.A.M.; writing—review and editing, D.M.C. and Ș.S. All authors have read and agreed to the published version of the manuscript.

**Funding:** This research received no external funding.

**Data Availability Statement:** Data are available on request from the corresponding author.

**Acknowledgments:** Andrei Ioan Indreş acknowledges the grand no. 06.46/01.10.2019 awarded by the Ministry of Education from Romania for completing his PhD studies.

**Conflicts of Interest:** The authors declare no conflicts of interest.

## References

1. Pierre, J.; Iervolino, F.; Farahani, R.D.; Piccirelli, N.; Levesque, M.; Therriault, D. Material extrusion additive manufacturing of multifunctional sandwich panels with load-bearing and acoustic capabilities for aerospace applications. *Addit. Manuf.* **2023**, *61*, 103344. [CrossRef]
2. Lurie, S.A.; Solyaev, Y.O.; Volkov-Bogorodskiy, D.B.; Bouznik, V.M.; Koshurina, A.A. Design of the corrugated-core sandwich panel for the arctic rescue vehicle. *Compos. Struct.* **2017**, *160*, 1007–1019. [CrossRef]
3. Baral, N.; Cartie, D.D.R.; Partridge, I.K.; Baley, C.; Davies, P. Improved impact performance of marine sandwich panels using through-thickness reinforcement: Experimental results. *Compos. Part B-Eng.* **2010**, *41*, 117–123. [CrossRef]
4. Cui, Y.; Hao, H.; Li, J.; Chen, W.; Zhang, X. Structural behavior and vibration characteristics of geopolymer composite lightweight sandwich panels for prefabricated buildings. *J. Build. Eng.* **2022**, *57*, 104872. [CrossRef]
5. Guo, H.; Yuan, H.; Zhang, J.; Ruan, D. Review of sandwich structures under impact loadings: Experimental, numerical and theoretical analysis. *Thin Walled Struct.* **2024**, *196*, 111541. [CrossRef]
6. Wang, B.; Wu, L.Z.; Ma, L.; Feng, J.C. Low-velocity impact characteristics and residual tensile strength of carbon fiber composite lattice core sandwich structures. *Compos. Part B-Eng.* **2011**, *42*, 891–897. [CrossRef]
7. Yang, B.; Wang, Z.; Zhou, L.; Zhang, J.; Tong, L.; Liang, W. Study on the low-velocity impact response and CAI behavior of foam-filled sandwich panels with hybrid facesheet. *Compos. Struct.* **2015**, *132*, 1129–1140. [CrossRef]
8. Sun, M.; Wowk, D.; Mechefske, C.; Alexander, E.; Kim, Y. Surface and honeycomb core damage in adhesively bonded aluminum sandwich panels subjected to low velocity impact. *Compos. Part B-Eng.* **2022**, *230*, 109506. [CrossRef]
9. Zhang, D.; Zhang, W.; Zhou, J.; Zheng, X.; Wang, J.; Liu, H. Numerical investigation of the low-velocity impact damage resistance and tolerance of composite laminates with preloads. *Aerosp. Sci. Technol.* **2023**, *142 Pt A*, 108650. [CrossRef]
10. Liu, K.; Kang, S.B.; Gao, S. Experimental and analytical study on impact response of stainless steel-aluminum foam-alloy steel sandwich panels. *Int. J. Impact Eng.* **2023**, *173*, 104661. [CrossRef]
11. Pan, X.; Chen, L.; Deng, J.; Zhao, W.; Jin, S.; Du, B.; Chen, Y.; Li, W.; Liu, T. Low velocity impact response of thermoplastic composite sandwich panels with the intersected corrugated core. *Compos. Struct.* **2023**, *304*, 117574. [CrossRef]
12. Zhang, W.; Li, J.; Wang, Z.; Li, K.; Bai, C.; Qin, Q. The influence of asymmetric faces on low-velocity impact failure of CFRP/aluminum foam composite sandwich beams. *Eng. Struct.* **2023**, *292*, 116574. [CrossRef]
13. Zhou, X.; Jing, L. Low-velocity impact response of sandwich panels with layered-gradient metal foam cores. *Int. J. Impact Eng.* **2024**, *184*, 104808. [CrossRef]
14. Zhu, X.; Li, W.; Du, Y.; Li, X.; Wang, W.; Zhang, K. Impact resistance of single-cell and multi-cell sandwich aluminum plates filled with aluminum foam. *Thin Walled Struct.* **2023**, *188*, 110789. [CrossRef]
15. Yang, P.; Shams, S.S.; Slay, A.; Brokate, B.; Elhajjar, R. Evaluation of temperature effects on low velocity impact damage in composite sandwich panels with polymeric foam cores. *Compos. Struct.* **2015**, *129*, 213–223. [CrossRef]
16. Tan, H.L.; He, Z.C.; Li, E.; Tan, X.W.; Cheng, A.G.; Li, Q.Q. Energy absorption characteristics of three layered sandwich panels with graded re-entrant hierarchical honeycombs cores. *Aerosp. Sci. Technol.* **2020**, *106*, 106073. [CrossRef]
17. Usta, F.; Turkmen, H.S.; Scarpa, F. Low velocity impact resistance of composite sandwich panels with various types of auxetic and non-auxetic core structures. *Thin Walled Struct.* **2021**, *163*, 107738. [CrossRef]

18. Zhang, G.; Ma, L.; Wang, B.; Wu, L. Mechanical behavior of CFRP sandwich structures with tetrahedral lattice truss cores. *Compos. Part B-Eng.* **2012**, *43*, 471–476. [CrossRef]
19. Zhang, G.; Wang, B.; Ma, L.; Wu, L.; Pan, S.; Yang, J. Energy absorption and low velocity impact response of polyurethane foam filled pyramidal lattice core sandwich panels. *Compos. Struct.* **2014**, *108*, 304–310. [CrossRef]
20. Sun, H.; Yuan, H.; Zhang, J.; Zhang, J.; Du, J.; Huang, W. Dynamic response of multilayer sandwich beams with foam-filled trapezoidal corrugated and foam cores under low-velocity impact. *Eng. Struct.* **2023**, *286*, 116080. [CrossRef]
21. Zhang, Z.; Lei, H.; Xu, M.; Hua, J.; Li, C.; Fang, D. Out-of-plane compressive performance and energy absorption of multi-layer graded sinusoidal corrugated sandwich panels. *Mater. Des.* **2019**, *178*, 107858. [CrossRef]
22. Sun, G.; Huo, X.; Wang, H.; Hazell, P.J.; Li, Q. On the structural parameters of honeycomb-core sandwich panels against low-velocity impact. *Compos. Part B-Eng.* **2021**, *216*, 108881. [CrossRef]
23. Sun, G.; Wang, E.; Wang, H.; Xiao, Z.; Li, Q. Low-velocity impact behavior of sandwich panels with homogeneous and stepwise graded foam cores. *Mater. Des.* **2018**, *160*, 1117–1136. [CrossRef]
24. Mat Daud, S.Z.; Lim, J.; Amir, M.; Kim, S.W. Enhancing impact energy absorption in composite sandwich structures through synergistic smart material integration. *Results Eng.* **2024**, *21*, 101902. [CrossRef]
25. Fan, Y.; Wang, Y. The effect of negative Poisson's ratio on the low-velocity impact response of an auxetic nanocomposite laminate beam. *Int. J. Mech. Mater. Des.* **2021**, *17*, 153–169. [CrossRef]
26. Hou, S.; Li, T.; Jia, Z.; Wang, L. Mechanical properties of sandwich composites with 3d-ărinted auxetic and non-auxetic lattice cores under low velocity impact. *Mater. Des.* **2018**, *160*, 1305–1321. [CrossRef]
27. Lu, H.; Wang, X.; Chen, T. Quasi-static bending response and energy absorption of a novel sandwich beam with a reinforced auxetic core under the fixed boundary at both ends. *Thin Walled Struct.* **2023**, *191*, 111011. [CrossRef]
28. Hosseinkhani, A.; Younesian, D.; Ranjbar, M.; Scarpa, F. Enhancement of the vibro-acoustic performance of anti-tetra-chiral auxetic sandwich panels using topologically optimized local resonators. *Appl. Acoust.* **2021**, *177*, 107930. [CrossRef]
29. Ngo, T.D.; Kashani, A.; Imbalzano, G.; Nguyen, K.T.; Hui, D. Additive manufacturing (3D printing): A review of materials. methods. applications and challenges. *Compos. Part B-Eng.* **2018**, *143*, 172–196. [CrossRef]
30. Wang, X.; Jiang, M.; Zhou, Z.; Gou, J.; Hui, D. 3D printing of polymer matrix composites: A review and prospective. *Compos. Part B-Eng.* **2017**, *110*, 442–458. [CrossRef]
31. Wu, Y.; Fang, J.; Wu, C.; Li, C.; Sun, G.; Li, Q. Additively manufactured materials and structures: A state-of-the-art review on their mechanical characteristics and energy absorption. *Int. J. Mech. Sci.* **2023**, *246*, 108102. [CrossRef]
32. Sarvestani, H.Y.; Akbarzadeh, A.H.; Niknam, H.; Hermenean, K. 3D printed architected polymeric sandwich panels: Energy absorption and structural performance. *Compos. Struct.* **2018**, *200*, 886–909. [CrossRef]
33. Wang, W.J.; Zhang, W.M.; Guo, M.F.; Yang, J.S.; Ma, L. Energy absorption characteristics of a lightweight auxetic honeycomb under low-velocity impact loading. *Thin Walled Struct.* **2023**, *185*, 110577. [CrossRef]
34. Li, C.; Shen, H.S.; Yang, J.; Wang, H. Low-velocity impact response of sandwich plates with GRC face sheets and FG auxetic 3D lattice cores. *Eng. Anal. Bound. Elem.* **2021**, *132*, 335–344. [CrossRef]
35. Lu, Q.; Qi, D.; Li, Y.; Xiao, D.; Wu, W. Impact energy absorption performances of ordinary and hierarchical chiral structures. *Thin Walled Struct.* **2019**, *140*, 495–505. [CrossRef]
36. Wei, L.; Zhao, X.; Yu, Q.; Zhang, W.; Zhu, G. In-plane compression behaviors of the auxetic star honeycomb: Experimental and numerical simulation. *Aerosp. Sci. Technol.* **2021**, *115*, 106797. [CrossRef]
37. Guo, M.F.; Yang, H.; Ma, L. 3D lightweight double arrow-head plate-lattice auxetic structures with enhanced stiffness and energy absorption performance. *Compos. Struct.* **2022**, *290*, 115484. [CrossRef]
38. Özen, I.; Çava, K.; Gedikli, H.; Alver, Ü.; Aslan, M. Low-energy impact response of composite sandwich panels with thermoplastic honeycomb and reentrant cores. *Thin Walled Struct.* **2020**, *156*, 106989. [CrossRef]
39. Gibson, L.G.; Ashby, M.F. *Cellular Solids. Structure and Properties*; Cambridge University Press: Cambridge, UK, 1997.
40. *ASTM D638-22*; Standard Test Method for Tensile Properties of Plastics. ASTM International: West Conshohocken, PA, USA, 2022.
41. Do Kweon, H.; Kim, J.W.; Song, O.; Oh, D. Determination of true stress-strain curve of type 304 and 316 stainless steels using a typical tensile test and finite element analysis. *Nucl. Eng. Technol.* **2021**, *53*, 647–656. [CrossRef]
42. Cetin, E.; Baykasoğlu, C. Energy absorption of thin-walled tubes enhanced by lattice structures. *Int. J. Mech. Sci.* **2019**, *157–158*, 471–484. [CrossRef]
43. Yu, T.X.; Xiang, Y.; Wang, M.; Yang, L. Key performance indicators of tubes used as energy absorbers. *Key Eng. Mat.* **2015**, *626*, 155–161. [CrossRef]
44. Moure, M.M.; Rubio, I.; Aranda-Ruiz, J.; Loya, J.A.; Rodríguez-Millán, M. Analysis of impact energy absorption by lightweight aramid structures. *Compos. Struct.* **2018**, *203*, 917–926. [CrossRef]